Euler-Helfrich problem for open vesicles bounded by elastic filaments

Chengyao Zhang and Xin Yi*
School of Mechanics and Engineering Science, Peking University, Beijing 100871, China

(Received 19 November 2025; accepted 6 February 2026; published 2 March 2026)

We develop a theoretical framework to elucidate the mechanics and morphogenesis of open vesicles coupled to boundary filaments, capturing their geometric, energetic, and mechanical interplay. Using a spherical harmonics parametrization and constrained energy minimization, we systematically explore equilibrium morphologies as functions of filament length, stiffness, and topology, as well as membrane spontaneous curvature, uncovering a rich spectrum of shapes and transitions. For open vesicles bounded by flexible closed filaments, increasing filament length or spontaneous curvature drives transitions from cuplike to stomatocyte and budded morphologies, both axisymmetric and nonaxisymmetric, with continuous and discontinuous regimes mapped in a phase diagram. For open vesicles partially bounded by open filaments, the coupled filament-membrane system exhibits more complex morphological evolution, including free edge stretching or contraction, localized filament bending, and opening expansion with increasing filament length. The derived force and moment balances at the vesicle edge connect local geometric quantities, such as filament and membrane curvatures, to filament internal forces and membrane tension, providing a direct mechanical interpretation of shape equilibria. Our results reveal how filament geometry, topology, and bending stiffness govern membrane shape transformations and establish a general mechanical framework for coupled filament-membrane systems, such as DNA-vesicle complexes and other filament-mediated membrane structures.

DOI: 10.1103/9byv-ndvs

I. INTRODUCTION

One-dimensional filaments and two-dimensional membranes or sheets are ubiquitous in biological systems, where their mechanical coupling governs morphogenesis, dynamics, stability, and functional organization across scales [1,2]. Cytoskeletal and membrane-bound protein filaments, such as actin, microtubules, dynamin, ESCRT-III, and Atg17, interact with lipid membranes to drive cellular shape transformations, division, and motility, enabling processes ranging from the platelet discoid-to-spherical transition during activation to membrane remodeling events such as tubulation, fission, scission, and autophagy [3–6]. Another prominent instance is the nuclear lamina, where a meshwork of lamin filaments couples with the nuclear envelope to govern nuclear morphology, stability, and the nucleation of pores or blebs [7–9].

Synthetic analogs, such as vesicles encapsulating actin networks and microtubules under different osmotic conditions, recapitulate essential aspects of cytoskeletal-membrane coupling, enabling the exploration of morphogenesis with reduced biochemical complexity [10–13]. Recent work has demonstrated that enclosed interacting filaments, driven by long-range repulsive forces, can induce dramatic and programmable vesicle shape transformations [14]. Extending to the tissue scale, the mechanical interplay between the gut tube and its anchoring mesenteric sheet drives the looping, chirality, and morphogenesis of the developing vertebrate intestine [15]. Together, these examples highlight a universal physical principle: The interaction between one- and two-dimensional soft structures underlies shape generation and stability in living and synthetic systems.

Recent advances in nanotechnology and synthetic biology now enable artificial filaments to be designed, fabricated, and manipulated with molecular precision. DNA nanotubes, peptide filaments, and protein chains can be engineered to bind, scaffold, or deform lipid membranes, allowing programmable control over membrane geometry and topology [16,17]. Traditionally, the mechanics of open vesicles have been modeled by assigning a prescribed line tension along the free edge [18–20], since open membranes are typically realized experimentally by introducing proteins or surfactants that stabilize the pore rim [21–23]. In such cases, the energetic contribution of the edge is proportional to its length, and the line tension effectively describes a one-dimensional boundary energy without bending stiffness.

However, emerging techniques now make it possible to functionalize membrane edges with filamentous or polymeric structures that endow the boundary with elasticity and shape adaptability [16,24,25]. This introduces a class of geometric-mechanical coupling, where the membrane curvature elasticity interacts with the bending resistance of the enclosing filament. A biologically relevant realization of this principle is found in scaffolded nanodiscs—discoidal lipid bilayers stabilized by encircling DNA or protein

*Contact author: xyi@pku.edu.cn

scaffolds [26]. In high-density lipoprotein particles, for instance, amphipathic apolipoproteins wrap around the bilayer edge, providing structural reinforcement and curvature control that resemble the elastic boundary considered here. Consequently, the open vesicle is transformed from a surface with a geometric edge into a composite elastic system in which both the membrane and the edge-bounded filament can deform and transmit forces, fundamentally modifying its mechanical equilibrium and morphological behavior.

To describe such systems, we develop the Euler-Helfrich framework—a coupled elastic model in which a deformable vesicle membrane is fully or partially bounded by a flexible filament. This formulation extends the classical Helfrich theory for lipid membranes [27] by introducing filament elasticity at the edge [28], in analogy with the Euler-Plateau problem [29,30], which describes elastic filaments bounding soap films governed by surface tension. In contrast to the Plateau system, dominated by positive surface tension and area minimization, the present problem involves membranes with finite bending rigidity and possibly negative membrane tension. These two features lead to qualitatively different mechanical behavior, including buckling-driven instabilities and nonminimal surface morphologies.

While a few recent theoretical studies have examined related Euler-Helfrich type systems [31–33], these efforts have primarily focused on mathematical generalizations rather than physically constrained membranes. In these models, the membrane area and filament length are treated as free parameters, unconstrained by surface inextensibility or filament stretchability, and the membrane tension is either prescribed *a priori* or not introduced. As a result, the membrane area and filament length can vary freely, effectively being relaxed in the energy minimization, rather than being fixed by physical constraints, and the resulting equilibria are therefore primarily geometric, favoring highly symmetric configurations such as smoothly deformed axisymmetric shapes. In contrast, membrane area conservation and filament length constraints cannot be alleviated by rescaling. Incorporating these constraints yields a mechanically constrained and physically consistent framework, and enables the emergence of nonaxisymmetric morphologies through the interplay among membrane curvature elasticity, edge tension, and filament confinement.

Building on this physically constrained framework, we analyze how the competition among three energetic mechanisms, membrane bending that favors smooth surfaces, filament bending that resists strong curvature, and line tension that drives edge contraction, determines the equilibrium morphology. We first formulate the elastic energy of the coupled filament-vesicle system, and then employ numerical energy minimization to systematically explore equilibrium morphologies by varying the filament stiffness and length together with the membrane spontaneous curvature and line tension. We quantify the morphological pathways of open vesicles with edge fully or partially bounded by elastic filaments, and reveal rich shape transitions—ranging from cuplike to stomatocyte and budded configurations, including nonaxisymmetric morphologies not reported previously. In parallel, the mechanical boundary conditions are derived analytically, linking the local filament curvature and torsion to the membrane tension and filament forces. Together, these results establish a theoretical framework for filament-membrane coupling, bridging the classical Helfrich and Euler-Plateau problems, and providing physical insight into how elastic boundaries regulate vesicle morphogenesis.

II. THEORETICAL MODELING

Consider an open vesicle whose edge $\mathscr{C}$ is either fully bounded by a closed filament loop or partially bounded by an open filament [Figs. 1(a) and 1(b)]. The filament is inextensible and has length L. The open vesicle has a fixed area $A = 4\pi R^2$, with R denoting the effective vesicle radius. In the case of the open filament, the segment of the vesicle edge exposed to the surrounding solvent is referred to as the free edge. The free edge is generally associated with a line tension γ, reflecting the excess free energy per unit length due to the unfavorable exposure of hydrophobic lipid chains. This line tension penalizes the presence of the free edge and drives its minimization, in competition with the deformations of the filament and the membrane. In the present formulation, the filament is geometrically constrained to lie on the vesicle edge and cannot detach from it. The filament-membrane coupling is therefore purely mechanical, mediated by geometric compatibility and force balance, without introducing any explicit adhesive interaction.

Employing the Helfrich formulation for the membrane [27] and a wormlike chain model with twist elasticity neglected for the filament [28], the total energy of the system, E_{tot}, consists of the membrane bending energy E_{m}, the filament bending energy E_{f}, and the free edge energy E_{edge}:

$$\begin{aligned} E_{\mathrm{tot}} &= E_{\mathrm{m}} + E_{\mathrm{f}} + E_{\mathrm{edge}}, \\ E_{\mathrm{m}} &= \frac{\kappa}{2}\int (2H + c_0)^2 \,\mathrm{d}A, \\ E_{\mathrm{f}} &= \frac{YI}{2}\int_0^L k^2 \,\mathrm{d}s, \\ E_{\mathrm{edge}} &= \gamma L_{\mathrm{edge}}. \end{aligned} \tag{1}$$

Here, κ, H, c_0, and $\mathrm{d}A$ denote the bending rigidity, local mean curvature, spontaneous curvature, and surface element of the vesicle membrane, respectively; YI (with Y the Young's modulus and I the moment of inertia), k, and $\mathrm{d}s$ denote the bending stiffness, local curvature, and length element of the filament, respectively; and γ and L_{edge} are the line tension and the unknown (*a priori* unspecified) length of the free edge, respectively. The membrane area A is constrained to be constant, and the surface tension $\sigma (= -\partial E_{\mathrm{tot}}/\partial A)$ arises as a Lagrange multiplier enforcing area conservation; consequently, it does not appear explicitly as an independent term in the energy functional in Eq. (1).

Throughout this work, the terms "flexible" and "stiff" filaments are used in a relative sense to distinguish different bending-rigidity regimes; in the terminology of polymer physics, the filaments considered here fall within the semiflexible regime.

Upon rescaling all lengths by R and all energies by κ, the system is governed by the dimensionless parameters characterizing the relative stiffness and length of the filament to the

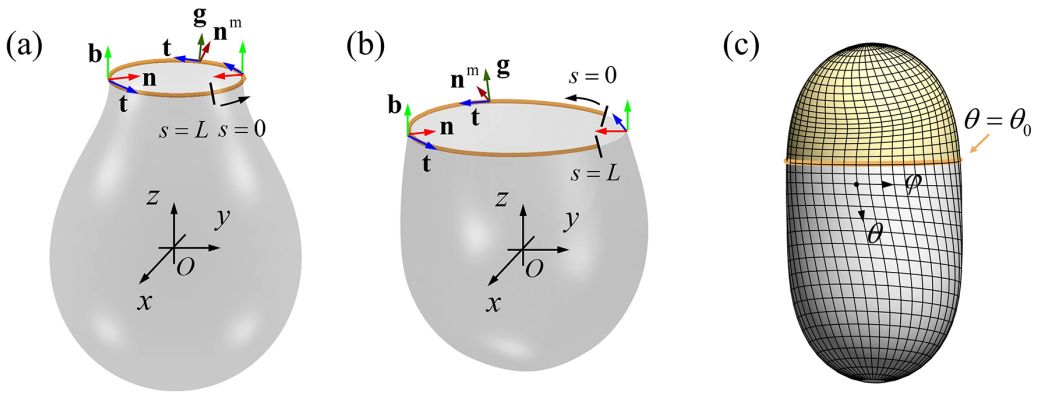

FIG. 1. Schematic of an open vesicle whose edge $\mathscr{C}$ is either fully bounded by a filament loop [panel (a)] or partially bounded by an open filament [panel (b)]. The filament is inextensible and has a total length L. The vesicle edge is represented as a space curve constrained to the membrane surface, with each point equipped with both a Frenet-Serret frame $\{\mathbf{t}, \mathbf{n}, \mathbf{b}\}$, consisting of the unit tangent vector $\mathbf{t}$, unit normal vector $\mathbf{n}$, and unit binormal vector $\mathbf{b}$ of the edge curve $\mathscr{C}$, and a Darboux frame $\{\mathbf{t}, \mathbf{g}, \mathbf{n}^{\mathrm{m}}\}$, adapted to the local membrane surface, with $\mathbf{g}$ the unit conormal vector and $\mathbf{n}^{\mathrm{m}}$ the unit surface normal vector. A Cartesian coordinate system O-xyz is introduced as a reference frame for system parametrization. (c) In the modeling framework, the open vesicle is obtained from a closed vesicle by assigning a vanishing bending rigidity to a designated membrane portion (light yellow), which is rendered transparent in the schematics in panels (a) and (b). The filament is positioned along a prescribed coordinate curve at polar angle $\theta = \theta_0$, spanning the azimuthal angle from $\varphi = 0$ to $\varphi = \varphi_0$ [with $\varphi_0 = 2\pi$ taken in panel (c) for illustration].

vesicle, as well as the line tension, such that

$$E_{\mathrm{tot}} = E_{\mathrm{tot}}\left(\frac{YI}{\kappa R}, \frac{L}{\pi R}, \frac{\gamma R}{\kappa}\right).$$

To model the shape of an open vesicle, we start from a closed vesicle and designate a membrane portion with vanishing bending rigidity [Fig. 1(c)]. This treatment renders the chosen portion incapable of resisting bending and thereby acts as an effective opening. In a Cartesian coordinate system, the vesicle surface is parametrized as $\mathbf{r}^{\mathrm{m}}(\theta, \varphi) = (x^{\mathrm{m}}, y^{\mathrm{m}}, z^{\mathrm{m}})$, whose components are expanded in spherical harmonics with θ and φ denoting the polar and azimuthal angles in spherical coordinates, respectively (Appendix A). For example, $x^{\mathrm{m}}(\theta, \varphi) = \sum_{l=0}^{l_{\max}} \sum_{m=-l}^{l} C_{lm}^{x}\, y_{lm}(\theta, \varphi)$, where C_{lm}^{x} is the expansion coefficient and $y_{lm}(\theta, \varphi)$ represents the real spherical harmonics indexed by integers l and m. The coordinates $y^{\mathrm{m}}(\theta, \varphi)$ and $z^{\mathrm{m}}(\theta, \varphi)$ can be expressed analogously to $x^{\mathrm{m}}(\theta, \varphi)$ by changing C_{lm}^{x} to C_{lm}^{y} and C_{lm}^{z}, respectively. For a closed vesicle, the angular domain is $\theta \in [0, \pi]$ and $\varphi \in [0, 2\pi]$. For an open vesicle, the domain is restricted to $\theta \in [\theta_0, \pi]$ and $\varphi \in [0, 2\pi]$, with θ_0 a prescribed constant polar angle. In our notation, a spherical vesicle of radius R possesses a mean curvature of $-1/R$; a positive c_0 corresponds to outward (convex) bending, while a negative c_0 indicates inward (concave) bending toward the vesicle interior.

The vesicle edge $\mathscr{C}$, treated as a space curve constrained to the membrane surface, is specified by a prescribed constant polar angle θ_0 and parametrized by $\mathbf{r}^{\mathrm{m}}(\theta_0, \varphi)$ with $\varphi \in [0, 2\pi]$. Since the filament is anchored along this edge, its centerline is expressed as $\mathbf{r}^{\mathrm{f}}(\varphi) = \mathbf{r}^{\mathrm{m}}(\theta_0, \varphi)$, where $\varphi \in [0, \varphi_0]$ and φ_0 denotes a prescribed azimuthal angle. For a closed filament loop, $\varphi_0 = 2\pi$ (Fig. 1). In the case of open filaments, the remaining free segment of the vesicle edge without a bounding filament is parametrized as $\mathbf{r}^{\mathrm{edge}}(\varphi) = \mathbf{r}^{\mathrm{m}}(\theta_0, \varphi)$ with $\varphi \in [\varphi_0, 2\pi]$.

Based on the parametrizations $\mathbf{r}^{\mathrm{m}}(\theta, \varphi)$, $\mathbf{r}^{\mathrm{edge}}(\varphi)$, and $\mathbf{r}^{\mathrm{f}}(\varphi)$, one can evaluate the geometrical characteristics and energy contributions of the open vesicle-filament system (Appendix A). For the vesicle, these include the mean curvature H, total area A, surface normal vector $\mathbf{n}^{\mathrm{m}}$, and bending energy E_{m}. For the filament, they comprise the curvature k, torsion τ, total length L, associated Frenet-Serret frame $\{\mathbf{t}, \mathbf{n}, \mathbf{b}\}$, and bending energy E_{f}.

The total energy of the filament-vesicle system E_{tot}, given in Eq. (1), is expressed in terms of a set of control parameters C_{lm}^{x}, C_{lm}^{y}, and C_{lm}^{z} as $E_{\mathrm{tot}}(C_{lm}^{x}, C_{lm}^{y}, C_{lm}^{z})$. The total number of these control variables is $3(l_{\max}+1)^2$, with $l_{\max} = 5$ in present calculations. To obtain the equilibrium morphology of the system, E_{tot} is minimized subject to geometric constraints, namely, fixed vesicle surface area A and fixed filament length L. The constrained optimization is carried out using the sequential quadratic programming method, which requires the gradients of both the energy and constraints with respect to the control points C_{lm}^{i} $(i = x, y, z)$. Upon convergence, the equilibrium system morphology is obtained for given values of $YI/(\kappa R)$, L/R, and $\gamma R/\kappa$. During the numerical optimization, the mechanical boundary conditions at the vesicle edge (Appendix B) emerge as natural boundary conditions associated with the stationarity of the energy functional, and thus are not imposed explicitly.

Once the filament geometry is obtained, the internal force $\mathbf{F}^{\mathrm{f}}$ and internal moment $\mathbf{M}^{\mathrm{f}}$ of the filament can be expressed as [34]

$$\mathbf{F}^{\mathrm{f}} = F_{\mathrm{t}}\mathbf{t} + F_{\mathrm{n}}\mathbf{n} + F_{\mathrm{b}}\mathbf{b}, \tag{2}$$

$$F_{\mathrm{t}} = YI\left(\beta - \frac{k^2}{2}\right), \quad F_{\mathrm{n}} = -YIk', \quad F_{\mathrm{b}} = -YIk\tau,$$

$$\mathbf{M}^{\mathrm{f}} = YIk\mathbf{b}, \tag{3}$$

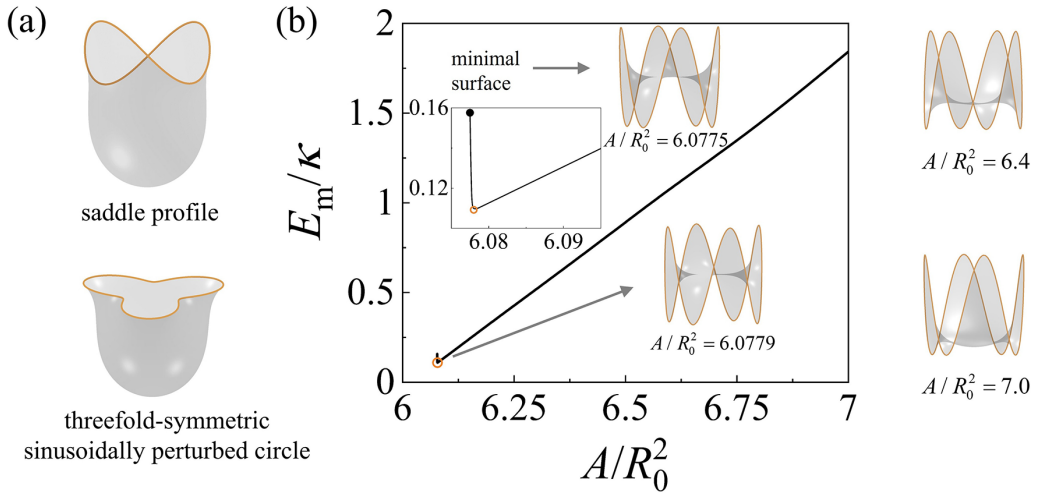

FIG. 2. Open vesicles with rigid edge-bounding filament loops. (a) Configurations with boundary filament curves resembling a saddle profile [$L/(\pi R) \approx 2.432$] and a threefold-symmetric sinusoidally perturbed circle [$L/(\pi R) \approx 2.608$]. (b) The membrane bending energy E_m as a function of the normalized membrane area A/R_0^2 for an open vesicle bounded by a dog-saddle filament loop [$L/(\pi R) \approx 5.611$].

where $\mathbf{t}$, $\mathbf{n}$, and $\mathbf{b}$ denote the unit tangent, principal normal, and binormal vectors, respectively. β is a constant Lagrange multiplier enforcing global filament inextensibility, determined through the constrained optimization, and k and τ represent the filament curvature and torsion defined in Eq. (A1). It is noted that the torsion τ quantifies the geometric nonplanarity of the filament centerline, rather than the elastic twist of the filament, which is not considered in this work. A positive F_t indicates a tensile tangential force, while positive F_n and F_b point along the normal $\mathbf{n}$ and binormal $\mathbf{b}$ directions, respectively.

Hereinafter, the prime ($'$) denotes differentiation with respect to the filament or free edge's arclength s, which is related to the azimuthal angle φ through the relation $\mathrm{d}s/\mathrm{d}\varphi = |\mathbf{r}^{\mathrm{f}}_{,\varphi}|$.

III. OPEN VESICLES BOUNDED BY CLOSED FILAMENT LOOPS

A. Open vesicles bounded by rigid filament loops of prescribed shapes

We first investigate open vesicle configurations constrained by fixed, rigid boundary filaments of prescribed shapes. This setup defines an Euler-Helfrich problem, in which the membrane minimizes bending energy while spanning specified boundary curves. To provide concrete examples and potential benchmark problems, we consider boundary geometries $\mathbf{r}^{\mathrm{f}} = (x^{\mathrm{f}}, y^{\mathrm{f}}, z^{\mathrm{f}})$ given by specific parametric forms, including a saddle profile, a polar plot with three lobes [Fig. 2(a)], and a dog-saddle profile [Fig. 2(b)]:

(1) the saddle profile

$$x^{\mathrm{f}} = R\cos t, \quad y^{\mathrm{f}} = R\sin t, \quad z^{\mathrm{f}} = R\sin t\cos t,$$

(2) the threefold-symmetric sinusoidally perturbed circle

$$x^{\mathrm{f}}/\cos t = y^{\mathrm{f}}/\sin t = R[1 + 0.4\sin(3t)], \quad z^{\mathrm{f}} = 0,$$

(3) the dog-saddle profile

$$x^{\mathrm{f}} = R_0\cos t, \quad y^{\mathrm{f}} = R_0\sin t, \quad z^{\mathrm{f}} = R_0[1 - 2\sin^2(2t)],$$

where $R\,(=\sqrt{A/(4\pi)})$ is the effective vesicle radius, R_0 is a length parameter, and $t \in [0, 2\pi]$ is the parametric variable of the filament curve.

Figure 2(b) illustrates the bending energy of the membrane spanning the dog-saddle profile as a function of the membrane area. The minimal-surface solution (indicated by the solid circle in the inset) corresponds to the configuration with the globally minimal area, whereas the bending energy attains its minimum at a slightly larger area and increases monotonically thereafter. This shows that the minimizers of the Euler-Plateau problem (area minimization) and the Euler-Helfrich problem (bending energy minimization) generally differ, even under identical boundary conditions.

B. Open vesicles bounded by flexible filament loops

1. Cases at vanishing spontaneous curvature ($c_0 = 0$)

We now consider open vesicles of vanishing spontaneous curvature bounded by flexible filament loops. Numerical results show that the equilibrium configuration is always axisymmetric regardless of filament stiffness (Fig. 3). At $L = 0$, the filament-free vesicle of vanishing spontaneous curvature is spherical with bending energy $E_m = 8\pi\kappa$. Increasing the edge-bounding filament length L drives a morphological sequence from nearly spherical to deep cup, shallow cup, and ultimately sheetlike shapes. At $L/(\pi R) = 4$, the open vesicle becomes a flat membrane. The morphological evolution is accompanied by a monotonic decrease in bending energy [Fig. 3(a)], indicating that the vesicle opening facilitates membrane bending energy relaxation. As the filament loop does not deform, only E_m is analyzed in Fig. 3(a). Similar transitions from spherical to cuplike and sheetlike morphologies have been reported in open vesicles with varying line tension arising from protein aggregation along the vesicle edge [21]; however, the underlying mechanism differs fundamentally, as our theoretical results in Fig. 3 pertain to vesicles bounded by filament loops rather than line tension-driven edge remodeling.

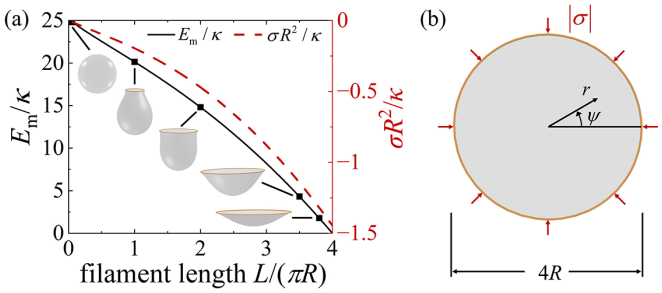

FIG. 3. Open vesicles bounded by filament loops of varying lengths. (a) Bending energy of the vesicle membrane E_m and membrane tension σ as functions of the normalized filament length $L/(\pi R)$. Negative σ corresponds to compressive membrane tension. (b) A circular membrane of radius $2R$ under uniform radial compression along the edge. Insets in panel (a): equilibrium configurations from numerical optimization.

Figure 3(a) shows that the membrane tension σ decreases monotonically with increasing $L/(\pi R)$. As $L/(\pi R) \to 0$, $\sigma \approx 0$, corresponding to a nearly stress-free spherical state. As the vesicle edge extends and the vesicle gradually flattens, σ becomes increasingly negative, reflecting that compressive membrane tension amplifies vesicle opening.

The tension profile in Fig. 3(a) is obtained from a full nonlinear analysis using the spherical harmonics parametrization combined with numerical optimization. To further rationalize these results, two limiting cases can be analyzed analytically. First, at $L = 0$, the vesicle is closed and adopts a spherical shape with bending energy $8\pi\kappa$. Since the bending energy of a spherical vesicle is independent of vesicle size, one finds $\sigma = -\partial E_{\rm tot}/\partial A = 0$. Second, at $L = 4\pi R$, the open vesicle becomes a flat membrane. In this case, any increase in membrane area necessarily produces deflection and bending energy, such that the membrane is under compressive tension corresponding to the critical load for buckling [Fig. 3(b)]. Based on the governing shape equation of the membrane under small-slope approximation [35,36], the critical membrane tension $\sigma_{\rm cr}$ can be derived as

$$\frac{\sigma_{\rm cr}R^2}{\kappa} = -\frac{j_{0,1}^2}{4} \approx -1.446, \tag{4}$$

in agreement with the numerical result in Fig. 3(a). Here, $j_{0,1} \approx 2.4048$ is the first positive root of J_0, the Bessel function of the first kind of order zero. The detailed derivation of Eq. (4) is provided in Appendix C.

2. *Effects of membrane spontaneous curvature on system behavior*

Figure 4 demonstrates the effect of membrane spontaneous curvature on vesicle morphologies at filament stiffness $YI/(\kappa R) = 1$. Depending on the filament length and membrane spontaneous curvature, the open vesicle could adopt cuplike shapes (as in Fig. 3), as well as stomatocyte and budded shapes [Fig. 4(a)]. The stomatocyte shape is characterized by an inward invagination with a narrow orifice, and the budded morphology consists of a round body connected to a round cap through a narrow membrane neck [Fig. 4(a)]. Both the cuplike and stomatocyte morphologies are axisymmetric, while the budded morphologies are axisymmetric at relatively small $L/(\pi R)$ but become nonaxisymmetric when $L/(\pi R)$ is large. The sequence of morphological transitions in Fig. 4(a) is more clearly understood in conjunction with the corresponding phase diagram in Fig. 4(b), which is mapped in terms of the normalized filament length $L/(\pi R)$ and spontaneous curvature c_0R.

Within the domain of the cuplike morphology, increasing c_0R drives a continuous evolution from a concave shape [e.g., morphology at $(1, -2)$ in Fig. 4(a)] to a convex shape [e.g., morphology at $(4/3, 1)$], mediated by local adjustments of membrane geometry near the filament constraint, as larger positive spontaneous curvature favors convex membrane bending.

For short filaments, further increase of c_0R drives a continuous transition from a cuplike vesicle to a stomatocyte [e.g., $(2/3, 2.1)$ and $(0.833, 2.2)$ in Fig. 4(a)], and eventually to a budded configuration [e.g., $(2/3, 2.8)$]. The stomatocyte-to-

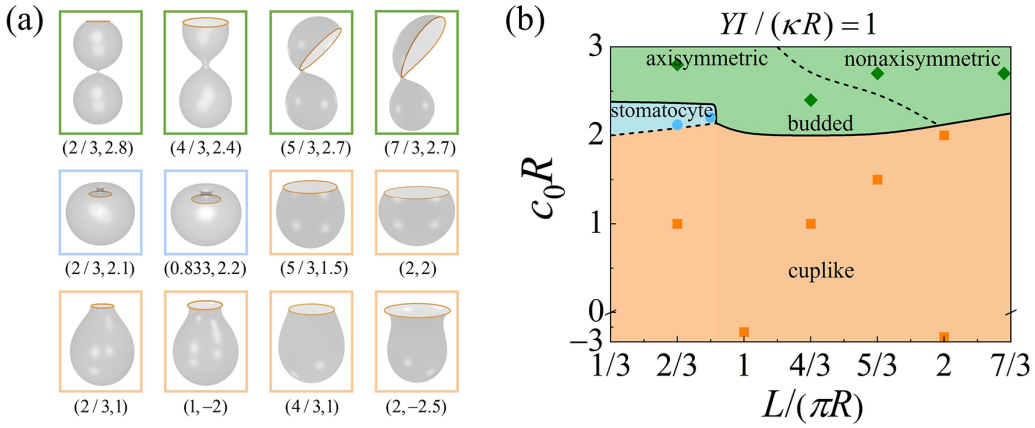

FIG. 4. Representative morphologies of open vesicles bounded by closed filaments at $YI/(\kappa R) = 1$ for different values of $(L/(\pi R),\ c_0R)$ [panel (a)], and the corresponding morphological phase diagram [panel (b)]. Solid (dashed) phase boundaries indicate discontinuous (continuous) morphological transitions. In panel (a), the values of $(L/(\pi R),\ c_0R)$ are given below each configuration. Both the cuplike and stomatocyte morphologies are axisymmetric, whereas the budded morphologies at relatively small $L/(\pi R)$ are axisymmetric but become nonaxisymmetric at relatively large $L/(\pi R)$. The axisymmetric budded shapes exhibit unduloidlike (neck-bulge) geometries.

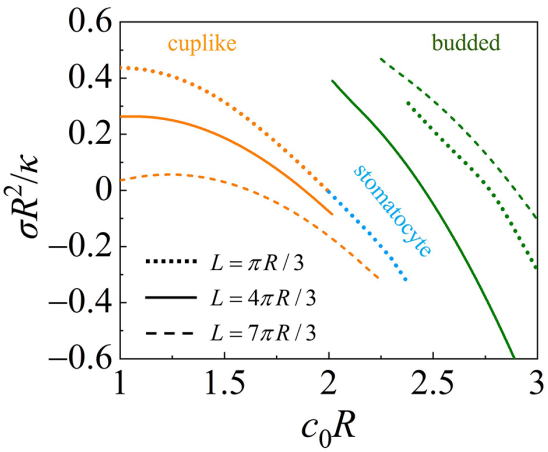

FIG. 5. Membrane tension σ as a function of normalized spontaneous curvature c_0R at $YI/(\kappa R)=1$ for $L/(\pi R)=1/3$, $4/3$, and $7/3$. Positive σ denotes tensile membrane tension. Sharp jumps in the σ-c_0 profiles mark the discontinuous morphological transitions.

budded transition is discontinuous [Fig. 4(b)], representing a first-order morphological switch triggered by a finite change in c_0R.

For relatively long filaments, the intermediate stomatocyte configuration is absent because the large opening precludes the formation of an inward-invaginated vesicle with a narrow orifice. Therefore, increasing c_0R drives a direct transition from a cuplike to a budded morphology [e.g., (2, 2) to (5/3, 2.7) and (7/3, 2.7) in Fig. 4(a)], again via a discontinuous transition [Fig. 4(b)]. In this regime, the long, flexible filament loop readily buckles out of plane under the strong filament-vesicle interaction [e.g., morphology at (7/3, 2.7) in Fig. 4(a)].

Accompanying the vesicle shape transitions, the membrane tension σ varies (Fig. 5). For short filaments [e.g., $L/(\pi R)=1/3$], σ decreases steadily with increasing c_0R as the vesicle progresses from a deep cup to a stomatocyte state, until a discontinuous transition to the budded morphology, where σ undergoes a sharp increase. For longer filaments [e.g., $L/(\pi R)=4/3$ and $7/3$], the vesicle evolves directly from a cup to a budded shape, again accompanied by a discontinuity in σ. Beyond the discontinuous transition to the budded shape, σ decreases again with increasing c_0R, as the budded morphology develops into a configuration consisting of a primary sphere connected to a spherical bud through a narrow, highly curved membrane neck.

To elucidate the mechanisms of shape transitions, we examine the system energy as a function of the spontaneous curvature for filament lengths $L/(\pi R)=1/3$, $4/3$, and $7/3$ at $YI/(\kappa R)=1$ (Fig. 6). For short filaments [e.g., $L/(\pi R)=1/3$ in Fig. 6(a)], the vesicle evolves from a cup toward a spherical shape with decreasing bending energy. Beyond a critical value of $c_0R\approx 1.9$, inward invagination forms a stomatocyte with a narrow neck, raising the bending energy. Further increase in c_0R yields an energetically favorable budded morphology, initially vertically asymmetric, which eventually develops into two nearly spherical, connected lobes corresponding to a global bending energy minimum. At higher c_0R, the size asymmetry between the lobes grows and the bending energy increases again.

For the normalized filament length beyond $L/(\pi R)\approx 0.86$, the intermediate stomatocyte stage vanishes, and the vesicle transitions directly from a cup to a budded morphology. Inward neck formation becomes geometrically infeasible as the long filament intersects the outer membrane contour, prompting an abrupt transition to outward-budded shapes.

At $L/(\pi R)=4/3$ and low spontaneous curvature, the vesicle adopts a concave cup [Fig. 6(b)]. Increasing c_0R drives a transition to a budded configuration of a nearly spherical vesicle connected to a shallow cap, representing a local bending energy minimum. Further increase in c_0R elongates the connected lobes, which gradually evolve into symmetric spherical buds at the global energy minimum. Beyond this point, lobe size asymmetry arises and bending energy increases.

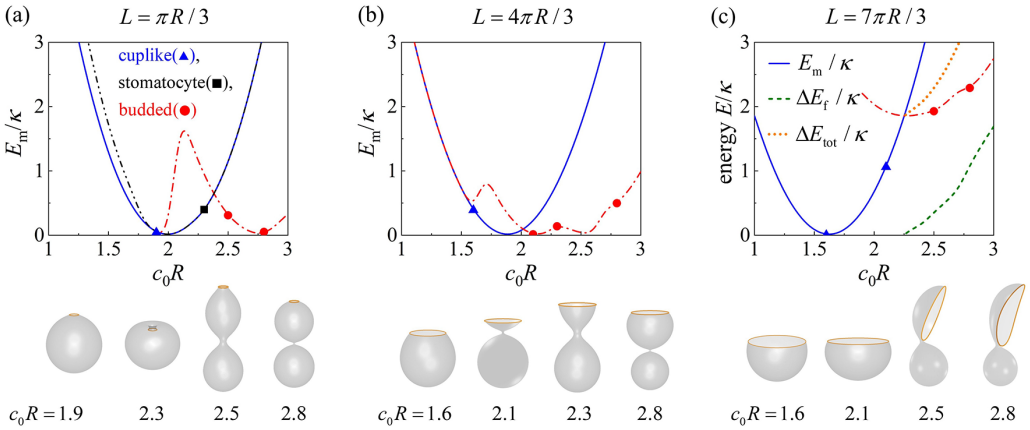

FIG. 6. Profiles of the system bending energy at $YI/(\kappa R)=1$ as a function of spontaneous curvature c_0R, together with selected equilibrium morphologies at the global energy minimum for $L/(\pi R)=1/3$ [panel (a)], $4/3$ [panel (b)], and $7/3$ [panel (c)]. Symbols on the energy curves correspond to the depicted vesicle configurations. In panels (a) and (b), the filament loops remain undeformed and circular, so only the membrane bending energy is examined. In panel (c), the filaments deform within the budded morphologies, and we introduce the energy variations $\Delta E_f=E_f-2\pi^2YI/L$ and $\Delta E_{tot}=E_m+\Delta E_f$ for the budded state, with the circular filament taken as the reference filament state.

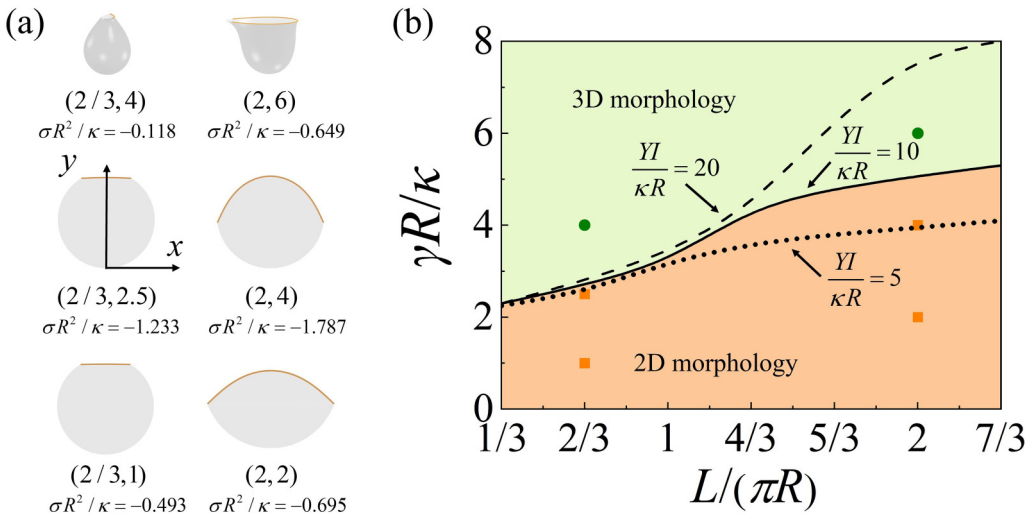

FIG. 7. Representative morphologies of open vesicles with $c_0 = 0$, partially bounded by open filaments at $YI/(\kappa R) = 10$, for different values of the normalized filament length $L/(\pi R)$ and line tension $\gamma R/\kappa$ [panel (a)], and the corresponding morphological phase diagram [panel (b)]. Phase boundaries at $YI/(\kappa R) = 5$, 10, and 20 in panel (b) mark discontinuous transitions from flat to curved membranes. In panel (a), the values of $(L/(\pi R),\ \gamma R/\kappa)$ are indicated below each configuration. All depicted morphologies are mirror symmetric.

For sufficiently long edge-bounding filaments, vesicles develop nonaxisymmetric budded morphologies, as indicated by tilted necks and filament buckling [Fig. 4(a)]. For $L/(\pi R) = 7/3$, the cup-shaped state persists over a broader range of spontaneous curvature [Fig. 6(c)], reflecting the additional geometric freedom of the extended edge. As $c_0 R$ increases, the vesicle undergoes a discontinuous transition to nonaxisymmetric buds. At high $c_0 R$ [e.g., 2.8 in Fig. 6(c)], the long filament buckles, producing tilted or twisted edges that drive nonaxisymmetric budding.

IV. OPEN VESICLES BOUNDED BY OPEN FILAMENTS

In contrast to closed filament loops, edge-bounding open filaments only partially constrain the vesicle edges, with their free ends stabilized by line tension. This relaxation of the global topological constraint provides the open vesicles with greater geometric freedom, allowing energy release through localized filament bending, membrane reshaping, and variations in edge length. As a result, open filaments allow open vesicles to explore remodeling pathways that both overlap with and differ from those induced by closed loops.

We first consider the case of zero membrane spontaneous curvature ($c_0 = 0$). In this case, a planar membrane has vanishing bending energy ($E_m = 0$) and thus represents the lowest-energy configuration. Consequently, flat membranes with edge-bounding filaments are possible at low line tension. To describe such configurations, we adopt a two-dimensional Cartesian coordinate system (x, y). In contrast, for membranes with nonzero spontaneous curvature, planar configurations incur finite bending energy and no longer minimize the energy; these cases will be discussed later.

The flat membrane edge is divided into a filament segment and a free edge segment. The local geometry of each segment is characterized by the tangent angle $\psi = \psi(s)$ as a function of arclength s. Accordingly, the coordinates (x, y) satisfy $\mathrm{d}x/\mathrm{d}s = \cos\psi$ and $\mathrm{d}y/\mathrm{d}s = \sin\psi$, and the membrane area is $A = (1/2)\oint(x\sin\psi - y\cos\psi)\,\mathrm{d}s$. The filament bending energy is $E_f = (YI/2)\int_0^L(\mathrm{d}\psi/\mathrm{d}s)^2\mathrm{d}s$, and the line tension energy of the free edge is $E_{edge} = \gamma L_{edge}$. As the free edge length L_{edge} is not known *a priori*, in numerical calculations we normalize its arclength as $l = s/L_{edge}$ with $l \in [0, 1]$, and express all quantities associated with the free edge in terms of l. The tangent angle functions $\psi(s)$ and $\psi(l)$ in the filament and the free edge segments, respectively, are approximated by cubic B-spline curves [37]. No continuity of ψ is enforced at the junctions between the filament and free edge. Upon constraints of membrane area A and filament length L, the equilibrium state of the flat configuration for given L/R and $\gamma R^2/(YI)$ is obtained via numerical optimization.

At high line tension, the free edge contracts markedly, constricting the vesicle opening and inducing three-dimensional system configurations. These shapes are represented using the spherical harmonics framework introduced in Sec. II, and their equilibrium morphologies are determined via numerical optimization.

Among all stable equilibria, whether two- or three-dimensional, the configuration corresponding to the global minimum of E_{tot} defines the most stable state. When two locally stable configurations possess identical total energy under the same parameters, the system lies at a configurational phase boundary, where both states are equally favorable and can coexist. This corresponds to a first-order (discontinuous) transition, enabling abrupt morphological switching accompanied by a finite change in the order parameter.

Figure 7 summarizes the equilibrium morphologies of open vesicles with edge-bounding open filaments, with representative shapes shown in Fig. 7(a) and the corresponding morphological phase diagram presented in Fig. 7(b). For planar configurations, the free membrane edge adopts a circular arc with radius of curvature $|\gamma/\sigma|$, as predicted by Eq. (B17), whereas the filament-bounded edge generally exhibits a nonuniform curvature profile, as governed by Eq. (B16). Here, the membrane tension σ acts equivalently

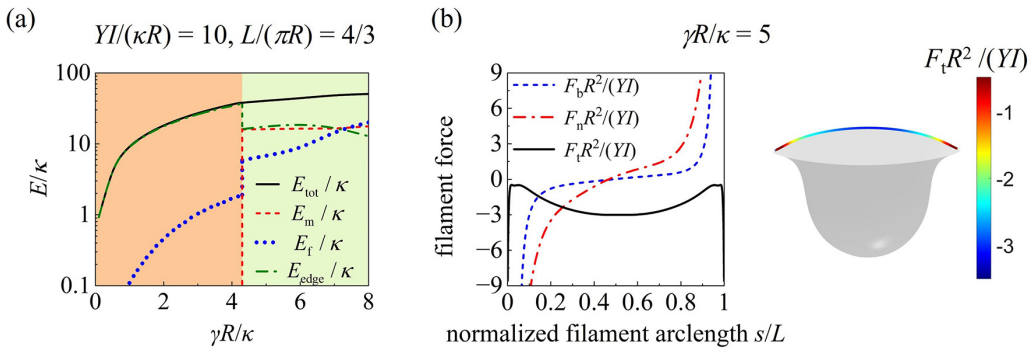

FIG. 8. (a) Profiles of the total energy $E_{\rm tot}$ and its components ($E_{\rm f}$, $E_{\rm m}$, $E_{\rm edge}$) as functions of normalized line tension $\gamma R/\kappa$. (b) Internal force components of the edge-bounding filament at $\gamma R/\kappa = 5$ and the corresponding system morphology. The vesicle membrane is of $c_0 = 0$. The filament stiffness and length are fixed at $YI/(\kappa R) = 10$ and $L/(\pi R) = 4/3$. Negative $F_{\rm t}$ indicates compressive tangential force, positive $F_{\rm n}$ is along the normal vector $\mathbf{n}$, and positive $F_{\rm b}$ aligns with the binormal vector $\mathbf{b}$ of the filament centerline.

as the in-plane pressure difference across the free membrane edge. Short, stiff filaments tend to remain nearly straight at weak line tension, giving rise to circular cap-shaped membranes [e.g., morphology at $(L/(\pi R), \gamma R/\kappa) = (2/3, 1)$ in Fig. 7(a)]. In contrast, longer filaments are more susceptible to bending [e.g., (2, 2) in Fig. 7(a)]. Increasing $\gamma R/\kappa$ amplifies deformation, as seen by comparing (2/3, 1) with (2/3, 2.5) and (2, 2) with (2, 4). Beyond a critical threshold of $\gamma R/\kappa$, stronger line tension overcomes filament stiffness more effectively, and the system undergoes a discontinuous transition into a three-dimensional cuplike shape [e.g., (2/3, 4) and (2, 6) in Fig. 7(a)]. High line tension also favors shortening of the free edge, effectively constricting the opening of the vesicle.

Beyond line tension, filament stiffness also modulates the transition. The two- to three-dimensional transition requires substantial filament bending and edge narrowing, which demand higher line tension for stiffer filaments and thus shift the phase boundary upward [Fig. 7(b)]. For short filaments, stiffness $YI/(\kappa R)$ has little influence since they remain nearly undeformed. For longer filaments, bending and the resulting edge narrowing become important, amplifying the impact of filament stiffness.

To elucidate the mechanical basis of vesicle shape evolution, we analyze the system energy as a function of line tension for a relatively stiff filament of intermediate length [Fig. 8(a)]. The two- to three-dimensional transition is marked by a sharp increase in membrane and filament bending energies, accompanied by a sudden drop in line tension energy, which reflects the shortening of the free membrane edge. At low line tension, the membrane remains nearly flat and the filament experiences minimal deformation; therefore, the line tension energy constitutes the dominant contribution to the system energy evolution. Beyond the morphological transition, the total energy and all its components increase gradually with line tension, reflecting the progressive bending of the filament, deformation of the membrane, and shortening of the edge required to accommodate higher tension.

Figure 8(b) presents the tangential, normal, and binormal force components $F_{\rm t}(s)$, $F_{\rm n}(s)$, and $F_{\rm b}(s)$ at $\gamma R/\kappa = 5$. The filament is predominantly under compressive tangential force, with large compression at both ends and the midsection. In contrast, the normal force $F_{\rm n}$ and binormal force $F_{\rm b}$ gradually increase from the filament central region toward the ends, reflecting the growing influence of curvature gradients and torsion near the ends.

For open vesicles with nonzero spontaneous curvature, planar configurations are no longer energetically favorable. Figure 9 illustrates system morphologies at line tension

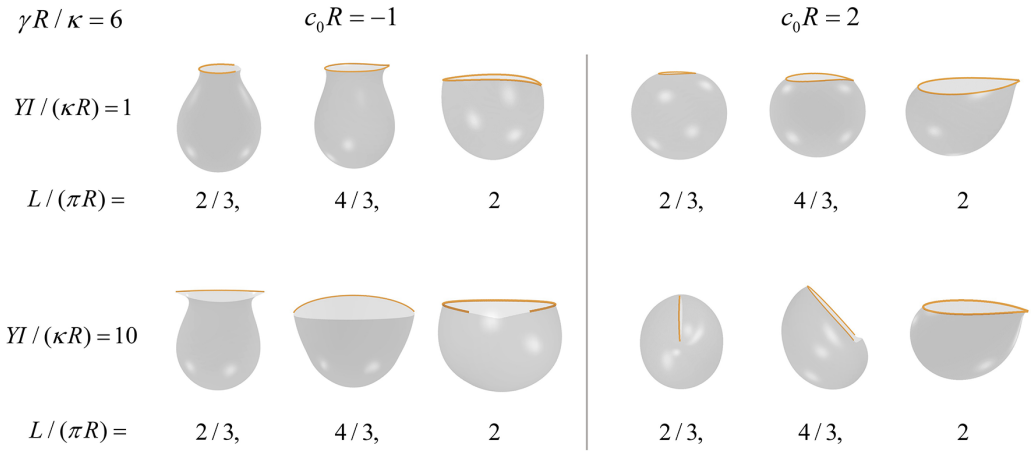

FIG. 9. Selected configurations of open vesicles with open filaments at line tension $\gamma R/\kappa = 6$ and normalized spontaneous curvature $c_0 R = -1$ and 2, comparing $YI/(\kappa R) = 1$ and 10 for different normalized filament lengths $L/(\pi R)$.

$\gamma R/\kappa = 6$ and normalized spontaneous curvature $c_0 R = -1$ and 2 for filaments of $YI/(\kappa R) = 1$ and 10.

The vesicles at $c_0 R = -1$ generally adopt cuplike shapes. For the flexible open filament [e.g., $YI/(\kappa R) = 1$], the filament strongly curves. With increasing filament length, the vesicle opening progressively widens and elongates, and the filament ends are drawn together. The filament then adopts a teardroplike configuration, consisting of a rounded swollen region that narrows smoothly toward the pinched end, such that the free edge is effectively suppressed. This evolution also drives a transition of the open filament from planar arrangements to out-of-plane morphologies. In contrast, stiff filaments [e.g., $YI/(\kappa R) = 10$] resist bending and straighten out. In this case, the vesicle opening could continue to expand, yet the free edge persists.

At $c_0 R = 2$, the short and flexible open filament [e.g., $YI/(\kappa R) = 1$] maintains an almost spherical vesicle shape. With increasing filament length, the boundary filament gradually bends out of plane, and the vesicle deviates from sphericity. For stiff filaments [e.g., $YI/(\kappa R) = 10$], the short boundary filament tends to elongate the vesicle along its longitudinal direction, while the opening contracts transversely; as the filament length increases, the opening expands.

V. DISCUSSION

A. Axisymmetric edge geometry and curvature conditions

For the open vesicle whose edge is either fully coupled with the filament or entirely free but subject only to a uniform line tension γ, the system can adopt axisymmetric configurations, as shown in Fig. 3 and reported in Refs. [18,19]. Using cylindrical coordinates (r, ψ, z), the axisymmetric membrane surface has its mean curvature H and Gaussian curvature K given by

$$H = -\frac{1}{2}\left(\frac{\mathrm{d}\alpha}{\mathrm{d}u} + \frac{\sin\alpha}{r}\right) \quad \text{and} \quad K = \frac{\sin\alpha}{r}\frac{\mathrm{d}\alpha}{\mathrm{d}u},$$

where α is the angle between the meridian tangent and the horizontal plane, and u is the meridional arclength. The geometric relations $\mathrm{d}r/\mathrm{d}u = \cos\alpha$ and $\mathrm{d}z/\mathrm{d}u = \sin\alpha$ hold.

Then, according to either Eqs. (B8) or (B13), we have

$$K = \frac{\sin\alpha}{r}\left(c_0 - \frac{\sin\alpha}{r}\right), \quad \text{on edge } \mathscr{C}.$$

For many configurations with $0 < \alpha < \pi$ at the edge, as long as $c_0 < (\sin\alpha/r)|_{\mathscr{C}}$, the local Gaussian curvature satisfies $K|_{\mathscr{C}} < 0$. This means that when the spontaneous curvature is too small to compensate the geometric curvature at the edge, the surface locally assumes a saddlelike form, consistent with Fig. 3 and previous numerical results [18,19].

B. Boundary conditions on free edge $\mathscr{C}_{\text{free-edge}}$

We now generally look at the three boundary conditions [Eqs. (B13)–(B15)] for the free edge segment $\mathscr{C}_{\text{free-edge}}$.

Equation (B13), $2H + c_0 = 0$, implies that the mean curvature H is constant along $\mathscr{C}_{\text{free-edge}}$. Consequently, the derivative of H along the edge tangent $\mathbf{t}$ must vanish:

$$\frac{\mathrm{d}H(\mathbf{r}^{\text{edge}}(s))}{\mathrm{d}s} = (\mathbf{r}^{\text{edge}})' \cdot \nabla_{\mathrm{S}} H = \mathbf{t} \cdot \nabla_{\mathrm{S}} H = 0, \quad \text{on } \mathscr{C}_{\text{free-edge}}. \tag{5}$$

At $c_0 = 0$, Eq. (B13) reduces to $H = 0$ on $\mathscr{C}_{\text{free-edge}}$, suggesting that the membrane near the edge behaves locally as a minimal surface.

Equation (B14), $\gamma k_{\mathrm{g}} - \sigma = 0$, shows that, at equilibrium, the free edge must maintain a constant geodesic curvature $k_{\mathrm{g}} = \sigma/\gamma$. If $\sigma > 0$ (tensile membrane tension) and $\gamma > 0$, then $k_{\mathrm{g}} > 0$, meaning that the edge bends along the conormal direction $\mathbf{g}$, forming a convex rim with radius of curvature $|\gamma/\sigma|$. Conversely, if $\sigma < 0$ (compressive tension), the free edge bends in the opposite direction, as demonstrated in Figs. 7(a), 8(b), and 9. When $\sigma = 0$, the free edge curve $\mathscr{C}_{\text{free-edge}}$ becomes geodesic ($k_{\mathrm{g}} = 0$).

Equation (B15), $\gamma k_{\mathrm{n}} + 2\kappa \mathbf{g} \cdot \nabla_{\mathrm{S}} H = 0$, indicates that, at equilibrium, if the local mean curvature H on $\mathscr{C}_{\text{free-edge}}$ is uniform along the $\mathbf{g}$ direction ($\mathbf{g} \cdot \nabla_{\mathrm{S}} H = 0$), then $\mathscr{C}_{\text{free-edge}}$ lies within the local tangent plane of the membrane ($k_{\mathrm{n}} = 0$). Otherwise, when H varies along $\mathbf{g}$, the free edge lifts or tilts relative to the membrane surface ($k_{\mathrm{n}} \neq 0$) to balance the normal force arising from the out-of-plane bending of the free edge relative to the local tangent plane.

If the line tension vanishes ($\gamma = 0$), Eq. (B14) immediately gives $\sigma = 0$. Moreover, Eq. (B15) reduces to $\mathbf{g} \cdot \nabla_{\mathrm{S}} H = 0$. Since the surface gradient of H can be decomposed as

$$\nabla_{\mathrm{S}} H = (\mathbf{g} \cdot \nabla_{\mathrm{S}} H)\mathbf{g} + (\mathbf{t} \cdot \nabla_{\mathrm{S}} H)\mathbf{t},$$

and at $\gamma = 0$ both components vanish, $\mathbf{g} \cdot \nabla_{\mathrm{S}} H = 0$ and $\mathbf{t} \cdot \nabla_{\mathrm{S}} H = 0$ [Eqs. (B15) and (5)], one obtains

$$\nabla_{\mathrm{S}} H = 0, \quad \text{on } \mathscr{C}_{\text{free-edge}}. \tag{6}$$

Equation (6) indicates that at $\gamma = 0$ the surface gradient of the mean curvature H vanishes on $\mathscr{C}_{\text{free-edge}}$, meaning H is locally constant in all directions tangent to the surface at the free edge.

C. Edge influencers

In the present formulation, the coupling between the filament and the membrane edge is purely mechanical, arising from geometric compatibility and force balance. In some synthetic or biological systems, filaments can also adhere to the vesicle edge through molecular binding or nonspecific attractions, introducing an additional energetic contribution that competes with filament bending and edge line tension. For systems containing multiple short filaments, strong adhesion may lead to multiple attachment sites along the edge, collectively stabilizing local edge configurations and suppressing large-amplitude filament deformations. Such adhesive interactions can be naturally incorporated into numerical simulations, extending the present framework to a broader class of filament-membrane systems. In this context, recent simulations on closed elastic shells with surface-adsorbed semiflexible polymers provide a valuable comparative perspective [38]. It is demonstrated that high concentrations of strongly adsorbed filaments can induce stable, nonspherical distortions and localized wrinkling, effects that parallel the

morphological transitions observed here under varying filament stiffness and boundary constraints. Furthermore, the potential for nematic ordering among long filaments to drive global ellipsoidal transitions suggests that extending our model to multiple interacting surface-constrained filaments could reveal complex and rich collective symmetry-breaking phenomena.

Another edge-effect contributor is the Gaussian curvature modulus $\bar{\kappa}$. In the present formulation, the influence of $\bar{\kappa}$, that is, the contribution of the $\bar{\kappa}K$ term in the integrand of the membrane bending energy E_{m}, has been neglected. For open membranes with fixed topology, the Gaussian curvature term reduces, via the Gauss-Bonnet theorem in differential geometry, to a boundary integral over the geodesic curvature plus a term proportional to the Euler characteristic of the surface—a topological invariant. In contrast, during fission or fusion events, in which the membrane topology changes discontinuously, the Gaussian term can contribute substantially to the overall energy variation.

Mechanically, $\bar{\kappa}$ enters the moment balance at the edge [39–42], thereby influencing the local membrane shape in the edge vicinity and, through geometric coupling, the overall vesicle morphology. Numerical studies show that the effect of $\bar{\kappa}$ is most pronounced near vesicle edges [18,19]; however, rigorous, general demonstrations that its influence is confined to a boundary region are lacking, and this conclusion remains largely empirical.

An additional edge-related effect involves torques transmitted through the vesicle edge. In the present model, the filament is treated as a bending-only wormlike chain, and twisting energy is neglected. For closed filament loops, twist is topologically constrained, as the total linking number is conserved in the absence of filament cutting or self-crossing, whereas open filaments may, in principle, accumulate twist if prescribed end rotations or external torques are applied at the edge. Incorporating twist elasticity would introduce an additional energetic penalty that could modify filament orientation and deformation in the edge vicinity. In particular, twisting energy may be partially relaxed through out-of-plane bending, thereby influencing membrane deformation near the edge.

VI. CONCLUSION

This theoretical study establishes a mechanical framework for open vesicles coupled to edge filaments, revealing how filament elasticity, length, and topology govern the vesicle morphogenesis. We identify equilibrium conditions and morphological pathways arising from the interplay of filament bending, membrane curvature elasticity, and edge line tension. The force and moment balances at the vesicle edge reveal the geometric coupling between filament curvature, torsion, and local membrane geometry, providing direct mechanical interpretation of the filament tangential force and membrane tension.

For closed filament loops with fixed shapes, the equilibrium membrane configuration governed by Helfrich energy differs from the minimal-surface configuration of the Plateau problem, highlighting a fundamental distinction between bending- and area-dominated energetics. When the filaments are elastic, the system undergoes transitions among cuplike, stomatocyte, and budded configurations, including nonaxisymmetric shapes not previously reported. Morphological phase diagrams, energy profiles, and membrane tension analyses further quantify these transitions.

For open filaments, relaxation of their topological constraint allows additional deformation modes, including edge stretching or contraction and localized filament bending. In membranes of zero spontaneous curvature, competition between filament bending and line tension drives the system transition from planar to three-dimensional shapes.

Overall, the framework offers a general route for analyzing coupled filament-membrane systems, with implications for protein-mediated vesicle openings, edge stabilization in lipid bilayers, and the design of artificial cellular systems with tunable boundaries—for example, using DNA filaments. The approach may be extended to include filament self-assembly or active forces to explore broader classes of shape remodeling phenomena in soft and biological membranes.

ACKNOWLEDGMENTS

This work was supported by the National Natural Science Foundation of China, Grants No. 12588301 and No. 12272004. We also gratefully acknowledge the High-Performance Computing Platform of Peking University for computational resources.

DATA AVAILABILITY

The data that support the findings of this article are not publicly available. The data are available from the authors upon reasonable request.

APPENDIX A: VESICLE AND FILAMENT PARAMETRIZATIONS

In a Cartesian coordinate system, the vesicle surface is parametrized as $\mathbf{r}^{\mathrm{m}}(\theta,\varphi) = (x^{\mathrm{m}}, y^{\mathrm{m}}, z^{\mathrm{m}})$, whose components are expanded in spherical harmonics as [11,43,44]

$$\mathbf{r}^{\mathrm{m}}(\theta,\varphi) = \begin{bmatrix} x^{\mathrm{m}}(\theta,\varphi) \\ y^{\mathrm{m}}(\theta,\varphi) \\ z^{\mathrm{m}}(\theta,\varphi) \end{bmatrix} = \begin{bmatrix} \sum_{l=0}^{l_{\max}} \sum_{m=-l}^{l} C^{x}_{lm} y_{lm}(\theta,\varphi) \\ \sum_{l=0}^{l_{\max}} \sum_{m=-l}^{l} C^{y}_{lm} y_{lm}(\theta,\varphi) \\ \sum_{l=0}^{l_{\max}} \sum_{m=-l}^{l} C^{z}_{lm} y_{lm}(\theta,\varphi) \end{bmatrix},$$

where θ and φ denote the polar and azimuthal angles in spherical coordinates. For the open vesicle, $\theta \in [\theta_0, \pi]$ and $\varphi \in [0, 2\pi]$, with θ_0 a prescribed polar angle. The expansion coefficients are denoted by C^{x}_{lm}, C^{y}_{lm}, and C^{z}_{lm}, and $y_{lm}(\theta,\varphi)$ represents the real spherical harmonics indexed by integers l and m, given by

$$y_{lm}(\theta,\varphi) = \begin{cases} \sqrt{2}\, M_{lm}\, P_{lm}(\cos\theta)\cos(m\varphi), & \text{if } m > 0, \\ M_{l0}\, P_{l0}(\cos\theta), & \text{if } m = 0, \\ \sqrt{2}\, M_{lm}\, P_{lm}(\cos\theta)\sin(-m\varphi), & \text{if } m < 0, \end{cases}$$

where $M_{lm} = \sqrt{(2l+1)(l-|m|)!/[4\pi(l+|m|)!]}$ and $P_{lm}(x) = \frac{(-1)^{|m|}}{2^l l!}(1-x^2)^{|m|/2}\frac{\mathrm{d}^{l+|m|}}{\mathrm{d}x^{l+|m|}}[(x^2-1)^l]$.

The local mean curvature H of the vesicle surface is

$$H = \frac{EN + GL - 2FM}{2(EG - F^2)},$$

where $E = \mathbf{r}^{\mathrm{m}}_{,\theta} \cdot \mathbf{r}^{\mathrm{m}}_{,\theta}$, $F = \mathbf{r}^{\mathrm{m}}_{,\theta} \cdot \mathbf{r}^{\mathrm{m}}_{,\varphi}$, and $G = \mathbf{r}^{\mathrm{m}}_{,\varphi} \cdot \mathbf{r}^{\mathrm{m}}_{,\varphi}$ are the coefficients of the first fundamental form, $L = \mathbf{r}^{\mathrm{m}}_{,\theta\theta} \cdot \mathbf{n}^{\mathrm{m}}$, $M = \mathbf{r}^{\mathrm{m}}_{,\theta\varphi} \cdot \mathbf{n}^{\mathrm{m}}$, and $N = \mathbf{r}^{\mathrm{m}}_{,\varphi\varphi} \cdot \mathbf{n}^{\mathrm{m}}$ are those of the second fundamental form, and $\mathbf{n}^{\mathrm{m}} = (\mathbf{r}^{\mathrm{m}}_{,\theta} \times \mathbf{r}^{\mathrm{m}}_{,\varphi})/|\mathbf{r}^{\mathrm{m}}_{,\theta} \times \mathbf{r}^{\mathrm{m}}_{,\varphi}|$ denotes the outward unit normal vector to the surface. For spherical vesicles, $H < 0$. Throughout, a comma in a subscript signifies partial derivative with respect to the corresponding coordinate (e.g., $\mathbf{r}^{\mathrm{m}}_{,\theta} = \partial \mathbf{r}^{\mathrm{m}}/\partial\theta$ and $\mathbf{r}^{\mathrm{m}}_{,\theta\varphi} = \partial^2 \mathbf{r}^{\mathrm{m}}/\partial\theta\partial\varphi$).

With the vesicle area element given by $\mathrm{d}A = \sqrt{EG - F^2}\,\mathrm{d}\theta\,\mathrm{d}\varphi = |\mathbf{r}^{\mathrm{m}}_{,\theta} \times \mathbf{r}^{\mathrm{m}}_{,\varphi}|\,\mathrm{d}\theta\,\mathrm{d}\varphi$, the bending energy E_{m} of the vesicle membrane in Eq. (1) becomes

$$E_{\mathrm{m}} = \frac{\kappa}{2}\int_0^{2\pi}\int_{\theta_0}^{\pi} (2H + c_0)^2 \sqrt{EG - F^2}\,\mathrm{d}\theta\,\mathrm{d}\varphi,$$

and the total area A of the vesicle is

$$A = \int_0^{2\pi}\int_{\theta_0}^{\pi} \left|\mathbf{r}^{\mathrm{m}}_{,\theta} \times \mathbf{r}^{\mathrm{m}}_{,\varphi}\right| \mathrm{d}\theta\,\mathrm{d}\varphi.$$

For the filament that is parametrized by $\mathbf{r}^{\mathrm{f}}(\varphi) = \mathbf{r}^{\mathrm{m}}(\theta_0, \varphi)$, its unit tangent, principal normal, and binormal vectors are denoted by $\mathbf{t}(\varphi)$, $\mathbf{n}(\varphi)$, and $\mathbf{b}(\varphi) = \mathbf{t} \times \mathbf{n}$, respectively, and given by

$$\mathbf{t} = \frac{\mathbf{r}^{\mathrm{f}}_{,\varphi}}{\left|\mathbf{r}^{\mathrm{f}}_{,\varphi}\right|}, \quad \mathbf{n} = \frac{\mathbf{r}^{\mathrm{f}}_{,\varphi} \times \mathbf{r}^{\mathrm{f}}_{,\varphi\varphi}}{\left|\mathbf{r}^{\mathrm{f}}_{,\varphi} \times \mathbf{r}^{\mathrm{f}}_{,\varphi\varphi}\right|},$$

and

$$\mathbf{b} = \frac{\left|\mathbf{r}^{\mathrm{f}}_{,\varphi}\right|}{\left|\mathbf{r}^{\mathrm{f}}_{,\varphi} \times \mathbf{r}^{\mathrm{f}}_{,\varphi\varphi}\right|}\mathbf{r}^{\mathrm{f}}_{,\varphi\varphi} - \frac{\mathbf{r}^{\mathrm{f}}_{,\varphi} \cdot \mathbf{r}^{\mathrm{f}}_{,\varphi\varphi}}{\left|\mathbf{r}^{\mathrm{f}}_{,\varphi}\right| \cdot \left|\mathbf{r}^{\mathrm{f}}_{,\varphi} \times \mathbf{r}^{\mathrm{f}}_{,\varphi\varphi}\right|}\mathbf{r}^{\mathrm{f}}_{,\varphi}.$$

The filament curvature k and torsion τ are given by

$$k = \frac{\left|\mathbf{r}^{\mathrm{f}}_{,\varphi} \times \mathbf{r}^{\mathrm{f}}_{,\varphi\varphi}\right|}{\left|\mathbf{r}^{\mathrm{f}}_{,\varphi}\right|^3}, \quad \tau = \frac{\left(\mathbf{r}^{\mathrm{f}}_{,\varphi} \times \mathbf{r}^{\mathrm{f}}_{,\varphi\varphi}\right) \cdot \mathbf{r}^{\mathrm{f}}_{,\varphi\varphi\varphi}}{\left|\mathbf{r}^{\mathrm{f}}_{,\varphi} \times \mathbf{r}^{\mathrm{f}}_{,\varphi\varphi}\right|^2}. \tag{A1}$$

With the filament length element $\mathrm{d}s = |\mathbf{r}^{\mathrm{f}}_{,\varphi}|\,\mathrm{d}\varphi$, the total filament length is then $L = \int_0^L \mathrm{d}s = \int_0^{\varphi_0} |\mathbf{r}^{\mathrm{f}}_{,\varphi}|\,\mathrm{d}\varphi$.

The bending energy E_{f} of the filament is

$$E_{\mathrm{f}} = \frac{YI}{2}\int_0^L k^2\,\mathrm{d}s = \frac{YI}{2}\int_0^{\varphi_0} \frac{\left|\mathbf{r}^{\mathrm{f}}_{,\varphi} \times \mathbf{r}^{\mathrm{f}}_{,\varphi\varphi}\right|^2}{\left|\mathbf{r}^{\mathrm{f}}_{,\varphi}\right|^5}\,\mathrm{d}\varphi.$$

In the case of open filaments, the length of the vesicle's free edge is $L_{\mathrm{edge}} = \int_{\varphi_0}^{2\pi} |\mathbf{r}^{\mathrm{edge}}_{,\varphi}|\,\mathrm{d}\varphi$.

APPENDIX B: EQUILIBRIUM MECHANICAL CONDITIONS AT THE VESICLE EDGE

In this section, we derive the mechanical boundary conditions at the vesicle edge $\mathscr{C}$. These boundary conditions are not imposed explicitly as constraints in the numerical optimization, but arise as natural boundary conditions associated with the stationarity of the total energy functional. Their derivation is included here for several important reasons. First, it ensures the completeness and internal consistency of the theoretical framework, as boundary conditions are a fundamental part of continuum mechanical analysis. Second, the resulting relations connect the filament's internal forces and the membrane tension to local geometric quantities (curvatures and torsion) at equilibrium, thus revealing how the mechanical response is encoded in the system geometry. Third, these analytical expressions provide a valuable reference for validating the numerical results and assessing the consistency of the computed equilibrium states.

1. Geometry and mechanical equilibrium of the vesicle edge

Depending on the filament topology, the vesicle edge $\mathscr{C}$ may be either fully bounded by a closed filament loop or partially bounded by an open filament. As a space curve, the intrinsic geometry of $\mathscr{C}$, characterized by curvature and torsion, is naturally described using the Frenet-Serret frame. Because the edge curve also lies on the membrane surface, its geometry is further constrained by the surface curvature, which is conveniently captured by the Darboux frame. Introducing both frames allows a consistent geometric description of the edge and is essential for formulating the mechanical boundary conditions at $\mathscr{C}$.

For either the filament-bounded edge segment ($\mathbf{r}^{\mathrm{f}}$ on $\mathscr{C}_{\mathrm{filament}}$) or the free edge segment without a bounding filament ($\mathbf{r}^{\mathrm{edge}}$ on $\mathscr{C}_{\mathrm{free\text{-}edge}}$), the unit tangent vector is $\mathbf{t} = (\mathbf{r}^{\mathrm{f}})'$ or $(\mathbf{r}^{\mathrm{edge}})'$. The unit principal normal vector is then defined as $\mathbf{n} = \mathbf{t}'/|\mathbf{t}'|$, and the unit binormal vector as $\mathbf{b} = \mathbf{t} \times \mathbf{n}$. Along $\mathscr{C}\,(= \mathscr{C}_{\mathrm{filament}} \cup \mathscr{C}_{\mathrm{free\text{-}edge}})$, these three mutually orthogonal vectors form a right-handed Frenet-Serret triad $\{\mathbf{t}, \mathbf{n}, \mathbf{b}\}$, which satisfies the Frenet-Serret formulas [45]

$$\mathbf{t}' = k\mathbf{n}, \quad \mathbf{n}' = -k\mathbf{t} + \tau\mathbf{b}, \quad \mathbf{b}' = -\tau\mathbf{n}, \tag{B1}$$

where $k = |\mathbf{t}'|$ is the curvature and $\tau = -\mathbf{b}' \cdot \mathbf{n}$ is the torsion, measuring the local deviation of the edge curve from its osculating plane spanned by $\mathbf{t}$ and $\mathbf{n}$. This geometrical torsion should be distinguished from the mechanical torsion of a twisted filament.

The Darboux frame $\{\mathbf{t}, \mathbf{g}, \mathbf{n}^{\mathrm{m}}\}$ along $\mathscr{C}$ is defined by the unit tangent vector $\mathbf{t}$, the unit normal vector $\mathbf{n}^{\mathrm{m}}$ of the vesicle surface, and the unit conormal vector $\mathbf{g} = \mathbf{n}^{\mathrm{m}} \times \mathbf{t}$. By differentiating the three mutually orthogonal vectors $\mathbf{t}$, $\mathbf{g}$, and $\mathbf{n}^{\mathrm{m}}$ with respect to the arclength s, and applying the Frenet-Serret formulas [Eq. (B1)], one obtains the Darboux formula [45]

$$\begin{aligned} \mathbf{t}' &= k_{\mathrm{g}}\mathbf{g} + k_{\mathrm{n}}\mathbf{n}^{\mathrm{m}}, \\ \mathbf{g}' &= -k_{\mathrm{g}}\mathbf{t} + \tau_{\mathrm{g}}\mathbf{n}^{\mathrm{m}}, \\ (\mathbf{n}^{\mathrm{m}})' &= -k_{\mathrm{n}}\mathbf{t} - \tau_{\mathrm{g}}\mathbf{g}, \end{aligned} \tag{B2}$$

where $k_{\mathrm{n}} = \mathbf{t}' \cdot \mathbf{n}^{\mathrm{m}}$ is the normal curvature, $k_{\mathrm{g}} = \mathbf{t}' \cdot \mathbf{g}$ is the geodesic curvature, and $\tau_{\mathrm{g}} = -(\mathbf{n}^{\mathrm{m}})' \cdot \mathbf{g}$ is the geodesic torsion of the edge curve. In the current choice for the curvilinear coordinates of the vesicle membrane (Appendix A), $\mathbf{n}^{\mathrm{m}}$ is the outward-pointing unit normal vector.

Substituting $\mathbf{t}' = k_{\mathrm{g}}\mathbf{g} + k_{\mathrm{n}}\mathbf{n}^{\mathrm{m}}$ into $\mathbf{t}' = k\mathbf{n}$ and $k\mathbf{b} = \mathbf{t} \times \mathbf{t}'$, we obtain

$$k\mathbf{n} = k_{\mathrm{g}}\mathbf{g} + k_{\mathrm{n}}\mathbf{n}^{\mathrm{m}} \quad \text{and} \quad k\mathbf{b} = -k_{\mathrm{n}}\mathbf{g} + k_{\mathrm{g}}\mathbf{n}^{\mathrm{m}}. \tag{B3}$$

Equation (B3) is useful in projecting the force and moment balances between the Frenet and Darboux representations.

For the Helfrich membrane with energy density given in Eq. (1), via variational analysis the force per unit length $\mathbf{f}^{\mathrm{m}}$ and moment per unit length $\mathbf{m}^{\mathrm{m}}$ due to the membrane

deformation are [39–42]

$$\mathbf{f}^{\mathrm{m}} = \kappa(2H + c_0)\tau_{\mathrm{g}}\mathbf{t} + 2\kappa(\mathbf{g}\cdot\nabla_{\mathrm{S}}H)\mathbf{n}^{\mathrm{m}} - \left[\sigma - \kappa(2H + c_0)\left(H - \frac{c_0}{2} - k_{\mathrm{n}}\right)\right]\mathbf{g}, \tag{B4}$$

$$\mathbf{m}^{\mathrm{m}} = -\kappa(2H + c_0)\mathbf{t}, \tag{B5}$$

where ∇_{S} denotes the surface gradient (the orthogonal projection of the standard gradient onto the tangent plane of the membrane) and $\mathbf{g}\cdot\nabla_{\mathrm{S}}H$ is the directional derivative of the mean curvature along the surface conormal $\mathbf{g}$.

For the filament-bounded edge segment ($\mathscr{C}_{\text{filament}}$), the static equilibrium of forces and moments along the filament read, respectively, [34]

$$(\mathbf{F}^{\mathrm{f}})' + \mathbf{f}^{\mathrm{m}} = \mathbf{0}, \tag{B6}$$

$$(\mathbf{M}^{\mathrm{f}})' + (\mathbf{r}^{\mathrm{f}})' \times \mathbf{F}^{\mathrm{f}} + \mathbf{m}^{\mathrm{m}} = \mathbf{0}, \tag{B7}$$

where $\mathbf{F}^{\mathrm{f}}$ and $\mathbf{M}^{\mathrm{f}}$ are the internal force and moment of the filament given in Eqs. (2) and (3), respectively.

The moment balance [Eq. (B7)], then reduces to $\mathbf{m}^{\mathrm{m}} = \mathbf{0}$, implying

$$2H + c_0 = 0, \qquad \text{on } \mathscr{C}_{\text{filament}}. \tag{B8}$$

Recalling Eqs. (B1)–(B3) and projecting the force balance [Eq. (B6)] onto the $\{\mathbf{t}, \mathbf{g}, \mathbf{n}^{\mathrm{m}}\}$ basis, on $\mathscr{C}_{\text{filament}}$, one obtains

$$YI\left[\left(\beta - \frac{k^2}{2} - \frac{k''}{k} + \tau^2\right)k_{\mathrm{g}} + \frac{(k^2\tau)'}{k^2}k_{\mathrm{n}}\right] - \sigma = 0, \tag{B9}$$

$$YI\left[\left(\beta - \frac{k^2}{2} - \frac{k''}{k} + \tau^2\right)k_{\mathrm{n}} - \frac{(k^2\tau)'}{k^2}k_{\mathrm{g}}\right] + 2\kappa\,\mathbf{g}\cdot\nabla_{\mathrm{S}}H = 0, \tag{B10}$$

where Eq. (B8) has been used. Here, β is the Lagrange multiplier enforcing filament inextensibility introduced in Eq. (2).

Equation (B8) represents moment balance along the $\mathbf{t}$ direction, and moments along $\mathbf{g}$ and $\mathbf{n}^{\mathrm{m}}$ vanish. Equations (B9) and (B10) represent force balance along $\mathbf{g}$ and $\mathbf{n}^{\mathrm{m}}$, respectively, while the force balance along $\mathbf{t}$ is automatically satisfied because of Eq. (B8). Equations (B8)–(B10) are consistent with previous results obtained via variational analysis [31,32].

For the free edge segment without a bounding filament ($\mathscr{C}_{\text{free-edge}}$), the static force and moment balances read, respectively,

$$(\gamma\mathbf{t})' + \mathbf{f}^{\mathrm{m}} = \mathbf{0}, \tag{B11}$$

$$\mathbf{m}^{\mathrm{m}} = \mathbf{0}. \tag{B12}$$

Following the similar procedure for the filament-bounded edge, the static force and moment balance equations (B11) and (B12) for the free edge segment yield

$$2H + c_0 = 0, \quad \text{on } \mathscr{C}_{\text{free-edge}}, \tag{B13}$$

$$\gamma k_{\mathrm{g}} - \sigma = 0, \quad \text{on } \mathscr{C}_{\text{free-edge}}, \tag{B14}$$

$$\gamma k_{\mathrm{n}} + 2\kappa\,\mathbf{g}\cdot\nabla_{\mathrm{S}}H = 0, \quad \text{on } \mathscr{C}_{\text{free-edge}}. \tag{B15}$$

Equation (B13) represents the moment balance along the edge tangent $\mathbf{t}$, while Eqs. (B14) and (B15) describe the force balances along $\mathbf{g}$ and $\mathbf{n}^{\mathrm{m}}$, respectively. Equations (B13)–(B15) are consistent with previous results obtained via variational analysis [40–42,46,47].

For a planar membrane configuration ($\tau = 0$ and $k_{\mathrm{n}} = 0$), Eqs. (B9) and (B14), respectively, reduce to

$$YI\left(\beta - \frac{k^2}{2} - \frac{k''}{k}\right)k - \sigma = 0, \quad \text{on } \mathscr{C}_{\text{filament}}, \tag{B16}$$

$$\gamma k + \sigma = 0, \quad \text{on } \mathscr{C}_{\text{free-edge}}. \tag{B17}$$

Equation (B16) corresponds to the two-dimensional Helfrich shape equation [48], also referred to as the generalized Young-Laplace equation, whereas Eq. (B17) represents the two-dimensional Young-Laplace equation with k as the signed curvature of the planar free edge. In Eq. (B17), the line tension γ and membrane tension σ play roles analogous to the surface tension and pressure difference, respectively, in the classical Young-Laplace relation.

All boundary conditions derived in this section are consistent with the numerical equilibrium solutions.

2. Filament tangential force and membrane tension

Subtracting Eq. (B10) multiplied by k_{g} from Eq. (B9) multiplied by k_{n} gives

$$\sigma = \frac{YI}{k_{\mathrm{n}}}(k^2\tau)' - 2\kappa\frac{k_{\mathrm{g}}}{k_{\mathrm{n}}}\,\mathbf{g}\cdot\nabla_{\mathrm{S}}H, \quad \text{on } \mathscr{C}_{\text{filament}}, \tag{B18}$$

where $k^2 = k_{\mathrm{g}}^2 + k_{\mathrm{n}}^2$ has been used. Equation (B18) demonstrates a remarkable mechanical balance: The edge geometry adjusts collectively so that the filament and membrane elasticity, edge curvature, and membrane curvature gradient exactly satisfy the constraint imposed by the uniform membrane tension σ.

At vanishing membrane bending rigidity ($\kappa = 0$), Eq. (B18) reduces to $\sigma = YI(k^2\tau)'/k_{\mathrm{n}}$ on $\mathscr{C}_{\text{filament}}$, consistent with the boundary equation for a liquid film spanning an elastic curve [29].

Adding Eqs. (B18) and (B10) multiplied by $k_{\mathrm{g}}/k_{\mathrm{n}}$, on $\mathscr{C}_{\text{filament}}$, one has

$$k_{\mathrm{g}}\beta = \left(\frac{k^2}{2} + \frac{k''}{k} - \tau^2\right)k_{\mathrm{g}} - \frac{k_{\mathrm{n}}}{k^2}(k^2\tau)' + \frac{\sigma}{YI},$$

from which, using Eq. (2), the tangential force component F_{t} along the filament can be obtained.

APPENDIX C: BUCKLING OF A CIRCULAR MEMBRANE UNDER UNIFORM COMPRESSION

At $L = 4\pi R$, the fully filament loop-bounded membrane becomes flat. Any increase in the membrane area would then induce an out-of-plane deflection. By integrating the equilibrium equation of the buckled membrane, the critical compressive membrane tension for buckling can be obtained as follows.

We recall the governing shape equation of the vesicle membrane of $c_0 = 0$ [48]:

$$\kappa\Delta_{\mathrm{S}}(2H) + 4\kappa H(H^2 - K) - 2\sigma H = 0, \tag{C1}$$

where Δ_{S} is the surface Laplacian (Laplace-Beltrami operator), K is the Gaussian curvature, and σ is the membrane

tension acting as the Lagrange multiplier to enforce fixed membrane area of the vesicle. The osmotic pressure term is omitted since we assume no pressure difference across the open vesicle membrane at equilibrium.

Under the small-slope approximation ($|\nabla z| \ll 1$ with z as the membrane deflection), $\Delta_S H \approx \nabla^2 H$ and $H \approx \pm(\nabla^2 z)/2$ with the sign depending on the chosen deflection direction. Then, Eq. (C1) reduces to

$$\kappa \nabla^4 z - \sigma \nabla^2 z = 0, \tag{C2}$$

where ∇^2 is the Laplace operator, $\nabla^4 = \nabla^2 \nabla^2$, and we have retained the leading order in H. Negative σ corresponds to a compressive membrane state. Equation (C2) is formally identical to the equilibrium equation for a buckled circular plate under uniform edge compression, where the flexural rigidity D of the plate is replaced by the membrane bending rigidity κ, and σ serves as the uniformly distributed compressive load [35,36].

Adopting a cylindrical coordinate system with radial distance r, azimuth angle ψ, and height [Fig. 3(b)], the Laplace operator in Eq. (C2) becomes

$$\nabla^2 = \frac{\partial^2}{\partial r^2} + \frac{1}{r}\frac{\partial}{\partial r} + \frac{1}{r^2}\frac{\partial^2}{\partial \psi^2}.$$

Assuming that the deflection surface $z(r, \psi)$ of the buckled membrane takes the separable angular form [36],

$$z(r, \psi) = w_n(r)\cos(n\psi), \quad (n = 0, 1, 2, \ldots), \tag{C3}$$

where n is the nodal number. The case $n = 0$ corresponds to the axisymmetric buckling mode.

Substituting Eq. (C3) into Eq. (C2) yields

$$\nabla_n^4 w_n - \frac{\sigma}{\kappa}\nabla_n^2 w_n = 0, \tag{C4}$$

where $\nabla_n^2 = \partial^2/\partial r^2 + r^{-1}\partial/\partial r - n^2/r^2$.

The general solution of Eq. (C4) consists of

$$w_0 = A_0 J_0\left(r\sqrt{\frac{|\sigma|}{\kappa}}\right) + B_0 Y_0\left(r\sqrt{\frac{|\sigma|}{\kappa}}\right) + C_0 + D_0 \ln r,$$

and for $n = 1, 2, \ldots$

$$w_n = A_n J_n\left(r\sqrt{\frac{|\sigma|}{\kappa}}\right) + B_n Y_n\left(r\sqrt{\frac{|\sigma|}{\kappa}}\right) + C_n r^n + \frac{D_n}{r^n},$$

where A_n, B_n, C_n, and D_n are constants of integration, and J_n and Y_n denote Bessel functions of the first and second kinds, respectively ($n \geqslant 0$).

Imposing membrane smoothness (finite displacement, slope, and curvature) at the membrane center $r = 0$ eliminates singular terms: $\ln r$ and the Y_0 term for $n = 0$ and r^{-n} and the Y_n for $n \geqslant 1$. Thus, the admissible solutions reduce to

$$w_n = A_n J_n\left(r\sqrt{\frac{|\sigma|}{\kappa}}\right) + C_n r^n, \quad (n = 0, 1, 2, \ldots).$$

At the boundary $r = 2R$, a simply supported condition is imposed, requiring vanishing bending moment, equivalently the mean curvature $H = 0$ (i.e., $\nabla^2 z = 0$). This condition leads to the buckling condition

$$J_n\left(2R\sqrt{\frac{|\sigma|}{\kappa}}\right) = 0, \quad (n = 0, 1, 2, \ldots).$$

The corresponding critical compressive tension is then

$$\sigma_{n,m} = -\kappa\left(\frac{j_{n,m}}{2R}\right)^2,$$

where $j_{n,m}$ is the mth positive root of $J_n = 0$. The least critical compressive tension is obtained for $n = 0$ and $m = 1$:

$$\sigma_{\mathrm{cr}} = -\kappa\left(\frac{j_{0,1}}{2R}\right)^2 \approx -1.446\frac{\kappa}{R^2}, \tag{C5}$$

where $j_{0,1} \approx 2.4048$ is the first positive root of J_0. Equation (C5) coincides with the numerical result in Fig. 3(a).

Since $n = 0$ corresponds to an axisymmetric deflection mode, the flat, filament-bordered membrane always buckles in an axisymmetric manner, consistent with the classical result for a simply supported circular plate under uniform compression [35,36].

At small slopes of the axisymmetric deflection, the membrane profile is given by

$$z(r) = w_0 = A_0 J_0\left(r\sqrt{\frac{|\sigma|}{\kappa}}\right) + C_0,$$

and the corresponding membrane area A is

$$A = 2\pi\int_0^\rho r\sqrt{1 + \left(\frac{\mathrm{d}z}{\mathrm{d}r}\right)^2}\,\mathrm{d}r \approx \pi\rho^2 + \pi\int_0^\rho r\left(\frac{\mathrm{d}z}{\mathrm{d}r}\right)^2\mathrm{d}r$$
$$= \pi\rho^2 + \frac{\pi\bar{\sigma}A_0^2}{2}\left[J_1^2(\sqrt{\bar{\sigma}}) - J_0(\sqrt{\bar{\sigma}})J_2(\sqrt{\bar{\sigma}})\right],$$

where

$$\bar{\sigma} = \frac{|\sigma|\rho^2}{\kappa} \quad \text{and} \quad \rho = \frac{L}{2\pi}.$$

Here, ρ is the radial size of the membrane projection on the r-ψ plane. For given A and σ, the coefficient A_0 can be determined.

Under the same small-slope assumption, the membrane bending energy E_{m} is

$$E_{\mathrm{m}} \approx \kappa\int(\nabla^2 z)^2\mathrm{d}A = \pi\kappa\int_0^\rho r\left(\frac{\mathrm{d}^2 z}{\mathrm{d}r^2} + \frac{1}{r}\frac{\mathrm{d}z}{\mathrm{d}r}\right)^2\mathrm{d}r$$
$$= \frac{\pi A_0^2\sigma^2\rho^2}{2\kappa}\left[J_0^2(\sqrt{\bar{\sigma}}) + J_1^2(\sqrt{\bar{\sigma}})\right]$$
$$= |\sigma|(A - \pi\rho^2)\frac{J_0^2(\sqrt{\bar{\sigma}}) + J_1^2(\sqrt{\bar{\sigma}})}{J_1^2(\sqrt{\bar{\sigma}}) - J_0(\sqrt{\bar{\sigma}})J_2(\sqrt{\bar{\sigma}})}.$$

The energy derivative with respect to the filament length at $L = 4\pi R$ is

$$\left.\frac{\mathrm{d}(E_{\mathrm{m}}/\kappa)}{\mathrm{d}(L/(\pi R))}\right|_{\rho=2R} = \frac{2\pi\sigma_{\mathrm{cr}}R^2}{\kappa} = -\frac{\pi(j_{0,1})^2}{2} \approx -9.084. \tag{C6}$$

The energy derivative in Eq. (C6) coincides with the numerical result in Fig. 3(a).

[1] D. Bray, *Cell Movements: From Molecules to Motility*, 2nd ed. (Garland Science, New York, 2001).

[2] X.-Q. Feng, B. Li, S. Z. Lin, M. Y. Wang, X. D. Chen, H. X. Zhang, and W. Fang, Mechano-chemo-biological theory of cells and tissues: Review and perspectives, Acta Mech. Sinica **41**, 625315 (2025).

[3] D. A. Fletcher and R. D. Mullins, Cell mechanics and the cytoskeleton, Nature (London) **463**, 485 (2010).

[4] A. H. Bahrami, M. G. Lin, X. Ren, J. H. Hurley, and G. Hummer, Scaffolding the cup-shaped double membrane in autophagy, PLoS Comput. Biol. **13**, e1005817 (2017).

[5] J. Agudo-Canalejo and R. Lipowsky, Domes and cones: Adhesion-induced fission of membranes by ESCRT proteins, PLoS Comput. Biol. **14**, e1006422 (2018).

[6] B. Meadowcroft, I. Palaia, A. K. Pfitzner, A. Roux, B. Baum, and A. Šarić, Mechanochemical rules for shape-shifting filaments that remodel membranes, Phys. Rev. Lett. **129**, 268101 (2022).

[7] C. M. Funkhouser, R. Sknepnek, T. Shimi, A. E. Goldman, R. D. Goldman, M. Olvera de la Cruz, Mechanical model of blebbing in nuclear lamin meshworks, Proc. Natl. Acad. Sci. USA **110**, 3248 (2013).

[8] Y. Turgay, M. Eibauer, A. Goldman, T. Shimi, M. Khayat, K. Ben-Harush, A. Dubrovsky-Gaupp, K. T. Sapra, R. D. Goldman, and O. Medalia, The molecular architecture of lamins in somatic cells, Nature (London) **543**, 261 (2017).

[9] D. Deviri, C. R. Pfeifer, L. J. Dooling, I. L. Ivanovska, D. E. Discher, and S. A. Safran, Scaling laws indicate distinct nucleation mechanisms of holes in the nuclear lamina, Nat. Phys. **15**, 823 (2019).

[10] T. Litschel, C. F. Kelley, D. Holz, M. A. Koudehi, S. K. Vogel, L. Burbaum, N. Mizuno, D. Vavylonis, and P. Schwille, Reconstitution of contractile actomyosin rings in vesicles, Nat. Commun. **12**, 2254 (2021).

[11] C. Shi, G. Zou, Z. Wu, M. Wang, X. Zhang, H. Gao, and X. Yi, Morphological transformations of vesicles with confined flexible filaments, Proc. Natl. Acad. Sci. USA **120**, e2300380120 (2023).

[12] A. Sciortino, H. A. Faizi, D. A. Fedosov, L. Frechette, P. M. Vlahovska, G. Gompper, and A. R. Bausch, Active membrane deformations of a minimal synthetic cell, Nat. Phys. **21**, 799 (2025).

[13] C. Shi, C. Zhang, Y. Fang, and X. Yi, Flexible filaments in vesicles with reduced volume: Anisotropic confinement and morphological response, J. Mech. Phys. Solids **206**, 106383 (2026).

[14] C. Zhang, G. Zou, Y. Fang, H. Gao, and X. Yi, Interacting filaments drive vesicle morphogenesis, Nat. Commun. **17**, 78 (2026).

[15] T. Savin, N. Kurpios, A. Shyer, P. Florescu, H. Liang, L. Mahadevan, and C. Tabin, The growth and form of the gut, Nature (London) **476**, 57 (2011).

[16] A. Fragasso, N. De Franceschi, P. Stömmer, E. O. van der Sluis, H. Dietz, and C. Dekker, Reconstitution of ultrawide DNA origami pores in liposomes for transmembrane transport of macromolecules, ACS Nano **15**, 12768 (2021).

[17] M. L. Daly, K. Nishi, S. J. Klawa, K. Y. Hinton, Y. Gao, and R. Freeman, Designer peptide–DNA cytoskeletons regulate the function of synthetic cells, Nat. Chem. **16**, 1229 (2024).

[18] T. Umeda, Y. Suezaki, K. Takiguchi, and H. Hotani, Theoretical analysis of opening-up transformations within single and two holes, Phys. Rev. E **71**, 011913 (2005).

[19] Z. Yao, R. Sknepnek, C. K. Thomas, M. Olvera de la Cruz, Shapes of pored membranes, Soft Matter **8**, 11613 (2012).

[20] Y. Liu, G. Zou, and H. Gao, Domain aggregation and associated pore growth in lipid membranes, ACS Nano **15**, 604 (2021).

[21] A. Saitoh, K. Takiguchi, Y. Tanaka, and H. Hotani, Opening-up of liposomal membranes by talin, Proc. Natl. Acad. Sci. USA **95**, 1026 (1998).

[22] F. Nomura, M. Nagata, T. Inaba, H. Hiramatsu, and K. Takiguchi, Capabilities of liposomes for topological transformation, Proc. Natl. Acad. Sci. USA **98**, 2340 (2001).

[23] R. J. C. Gilbert, M. Dalla Serra, C. J. Froelich, M. I. Wallace, and G. Anderluh, Membrane pore formation at protein–lipid interfaces, Trends Biochem. Sci. **39**, 510 (2014).

[24] H. G. Franquelim, H. Dietz, and P. Schwille, Reversible membrane deformations by straight DNA origami filaments, Soft Matter **17**, 276 (2021).

[25] J. Zhu, Z. A. McDargh, F. Li, S. S. Krishnakumar, J. E. Rothman, and B. O'Shaughnessy, Synaptotagmin rings as high-sensitivity regulators of synaptic vesicle docking and fusion, Proc. Natl. Acad. Sci. USA **119**, e2208337119 (2022).

[26] I. G. Denisov and S. G. Sligar, Nanodiscs in membrane biochemistry and biophysics, Chem. Rev. **117**, 4669 (2017).

[27] W. Helfrich, Elastic properties of lipid bilayers: Theory and possible experiments, Z. Naturforsch. C **28**, 693 (1973).

[28] P. J. Flory, *Statistical Mechanics of Chain Molecules* (Hanser Publishers, Munich, 1988).

[29] L. Giomi and L. Mahadevan, Minimal surfaces bounded by elastic lines, Proc. R. Soc. A **468**, 1851 (2012).

[30] A. Biria and E. Fried, Buckling of a soap film spanning a flexible loop resistant to bending and twisting, Proc. R. Soc. A **470**, 20140368 (2014).

[31] A. Biria, M. Maleki, and E. Fried, Continuum theory for the edge of an open lipid bilayer, Adv. Appl. Mech. **46**, 1 (2013).

[32] B. Palmer and Á. Pámpano, Minimizing configurations for elastic surface energies with elastic boundaries, J. Nonlinear Sci. **31**, 23 (2021).

[33] B. Palmer and Á. Pámpano, The Euler–Helfrich functional, Calc. Var. **61**, 79 (2022).

[34] L. D. Landau and E. M. Lifshitz, *Theory of Elasticity* (Butterworth-Heinemann, New York, 1986), 3rd ed.

[35] A. Nádai, Über das ausbeulen von kreisförmigen platten, Z. Ver. Dtsch. Ing. **59**, 169 (1915).

[36] N. Yamaki, Buckling of a thin annular plate under uniform compression, J. Appl. Mech. **25**, 267 (1958).

[37] M. Wang and X. Yi, Bulging and budding of lipid droplets from symmetric and asymmetric membranes: Competition between membrane elastic energy and interfacial energy, Soft Matter **17**, 5319 (2021).

[38] H. A. Hameed, J. Paturej, and A. Erbaş, Shape spectra of elastic shells with surface-adsorbed semiflexible polymers, Soft Matter **22**, 234 (2026).

[39] R. Capovilla and J. Guven, Stresses in lipid membranes, J. Phys. A: Math. Gen. **35**, 6233 (2002).

[40] Z. C. Tu and Z.-C. Ou-Yang, A geometric theory on the elasticity of bio-membranes, J. Phys. A: Math. Gen. **37**, 11407 (2004).

[41] M. Deserno, Fluid lipid membranes: From differential geometry to curvature stresses, Chem. Phys. Lipids **185**, 11 (2015).

[42] P. Yang, Q. Du, and Z. C. Tu, General neck condition for the limit shape of budding vesicles, Phys. Rev. E **95**, 042403 (2017).

[43] K. Khairy and J. Howard, Minimum-energy vesicle and cell shapes calculated using spherical harmonics, Soft Matter **7**, 2138 (2011).

[44] C. Zhang, Y. Fang, C. Shi, H. Yuan, and X. Yi, Stretching transition of vesicles with confined filament loops: Morphological evolution with filament distortion and reorientation, Giant **17**, 100233 (2024).

[45] H. W. Guggenheimer, *Differential Geometry* (Dover Publications, New York, 1977).

[46] R. Capovilla, J. Guven, and J. A. Santiago, Lipid membranes with an edge, Phys. Rev. E **66**, 021607 (2002).

[47] Z. C. Tu and Z.-C. Ou-Yang, Lipid membranes with free edges, Phys. Rev. E **68**, 061915 (2003).

[48] Z.-C. Ou-Yang and W. Helfrich, Bending energy of vesicle membranes: General expressions for the first, second, and third variation of the shape energy and applications to spheres and cylinders, Phys. Rev. A **39**, 5280 (1989).